Mechanical and topographic factors influencing lava dome growth and collapse

Claire Harnett, Michael Heap

To cite this version:

Mechanical and topographic factors influencing lava dome growth and collapse

Claire E. Harnett [a,*], Michael J. Heap [b,c]

[a] School of Earth Sciences, University College Dublin, Dublin, Ireland
[b] Université de Strasbourg, CNRS, Institut Terre et Environnement de Strasbourg, UMR 7063, 5 rue Descartes, Strasbourg F-67084, France
[c] Institut Universitaire de France (IUF), 1 rue Descartes, Paris 75231, France

ABSTRACT

Lava dome collapse hazards are intimately linked with their morphology and internal structure. We present new lava dome emplacement models that use calibrated rock strengths and allow material behaviour to be simulated for three distinct units: (1) a ductile, fluid core; (2) a solid upper carapace; and (3) disaggregated talus slopes. We first show that relative proportions of solid and disaggregated rock depend on rock strength, and that disaggregated talus piles can act as an unstable substrate and cause collapse, even in domes with a high rock strength. We then simulate sequential dome emplacement, demonstrating that renewed growth can destabilise otherwise stable pre-existing domes. This destabilisation is exacerbated if the pre-existing dome has been weakened following emplacement, e.g., through processes of hydrothermal alteration. Finally, we simulate dome growth within a crater and show how weakening of crater walls can engender sector collapse. A better understanding of dome growth and collapse is an important component of hazard mitigation at dome-forming volcanoes worldwide.

1. Introduction

Lava domes pose a significant hazard when they become unstable and collapse, generating rockfalls, debris avalanches and pyroclastic density currents (Calder et al., 2002). Lava domes can also affect the overall eruptive dynamics of a volcano, by affecting local stress fields and by restricting outgassing. The local stress effects from a resident lava dome can influence magma ascent direction (Lavallée et al., 2012) and magma ascent rate (Zorn et al., 2019), whilst rapid removal of dome material can release volatiles from an incompletely degassed magma and lead to rapid decompression of the hot, fluid dome core and thus cause explosive activity (Alidibirov and Dingwell, 1996; Voight et al., 2006; Watts et al., 2002; Woods et al., 2002). Lava domes can also encourage pore pressure augmentation within and beneath the dome by inhibiting the escape of exsolved magmatic volatiles, a process thought to promote explosive volcanic activity (Ball et al., 2015; Collinson and Neuberg, 2012; Heap et al., 2019; Stix, 1993; Taisne and Jaupart, 2008; Voight and Elsworth, 2000).

Lava dome hazards are highly dependent on dome morphology (Wang et al., 2015), which is predominantly determined by the structure and material properties (such as rock strength) of the dome, as well as the topographic structures that exist in the vicinity of the volcanic vent, e.g., pre-existing domes or crater geometry. These topographic structures are also vulnerable to alteration due to the efficient circulation of hydrothermal fluids (Byrdina et al., 2017; Ghorbani et al., 2018; Rosas-Carbajal et al., 2016), a process that can influence their material properties, including strength (Cecchi et al., 2004; del Potro and Hürlimann, 2009; Heap et al., 2019; Heap et al., 2021a; Reid et al., 2002; Voight and Elsworth, 1997). Therefore, for a more complete understanding of dome stability hazards, one must consider dome structure, rock strength, and existing topographic features.

Lava dome growth and morphology has been investigated using various modelling methods. Early analogue models investigated both Newtonian (e.g., Huppert et al., 1982) and Bingham rheologies (e.g., Blake, 1990), with later models also considering the effect of cooling on dome morphology (e.g., Fink and Bridges, 1995; Griffiths and Fink, 1993). A key conclusion from the later studies was that future modelling methods for lava dome growth should include formation of an 'outer crust' (Fink and Griffiths, 1998; Griffiths and Fink, 1993). More recently, a suite of modelling studies used the Finite Element Method (FEM) to simulate lava dome growth, considering an independently deformable talus region for the first time (Bourgouin et al., 2007; Hale, 2008; Hale et al., 2007). Hale (2008) described lava dome growth as occurring on two distinct timescales: (1) continuous expansion due to magma addition; and (2) readjustment of the talus material that has become detached from the main body of the dome. These FEM models were the

* Corresponding author.
E-mail address: harnettclaire@gmail.com (C.E. Harnett).

first to infer complex morphology of the rheological interface that exists between the frictionless, ductile lava dome core, and an outer friction-controlled talus.
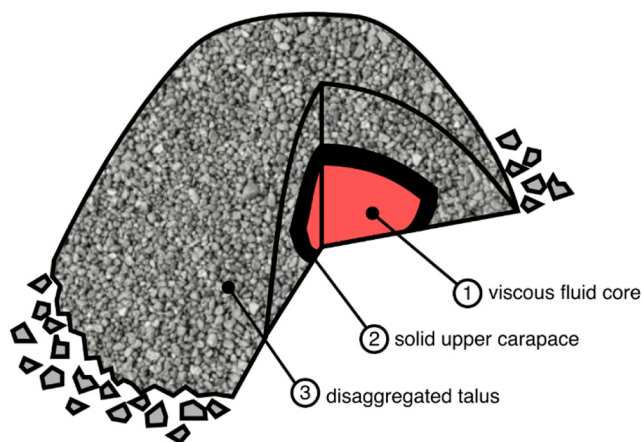
More recent Discrete Element Method (DEM) models of lava dome growth (Harnett et al., 2020; Harnett et al., 2018; Walter et al., 2019) also simulated a simplified internal dome structure. These models were, however, able to additionally simulate the short term, non-equilibrium nature of rockfalls that had previously been approximated as a critical-angle problem (Hale et al., 2009a, 2009b). Observations, however, suggest that the internal structure of a dome is more complex than reflected in existing models and likely comprises tripartite partitioning of mass and energy (Calder et al., 2015; Huppert et al., 1982; Szepesi et al., 2019; Wadge et al., 2009) into the following structural units: (1) a primarily fluid and viscous lava core; (2) an 'upper carapace' that acts as solid and coherent lava; and (3) talus that has accumulated through rockfalls and disaggregation of the lava core (Fig. 1). This distinction between the carapace and the talus has not been captured in previous computational models, but is incorporated in the new models presented here. The terms 'solid carapace' and 'disaggregated talus' are used throughout this article to refer to (2) and (3), respectively. Full understanding of *both* the solid carapace and disaggregated talus portions of a lava dome is key for considering advancement and stability of the dome, as the disintegration of carapace to form talus slopes provides stabilising confinement to the fluid dome core (Tuffen et al., 2013).

In this contribution, we present a suite of models that (1) incorporate different material behaviours for the coherent and disaggregated solid portions of the dome, allowing for more complex morphologies and structures to be simulated; (2) calibrate the computational models to incorporate realistic rock strengths and assess the effect of rock strength on dome stability; (3) investigate the effect of sequential dome growth on dome stability; and (4) investigate crater wall strength as a controlling factor in dome stability. A better understanding of dome growth and collapse is an important component of hazard mitigation at dome-forming volcanoes worldwide (Harnett et al., 2019b; Ogburn et al., 2015).

2. Methods

2.1. Model setup

A complete description of the model setup is provided by Harnett et al. (2018). In brief, the two-dimensional model uses the discrete element method (DEM), a particle-based methodology that calculates an explicit solution to Newton's laws of motion and updates the force and moment per particle per timestep, thus computing a displacement for each particle. The DEM is particularly pertinent for modelling lava dome emplacement and stability as it allows for the visualisation of localised strain within a lava dome that cannot be elucidated from satellite or photographic monitoring. In all models, a 'batch' of magma is extruded from a conduit with a diameter of 30 m, and 'batches' continue to be generated at depth during dome growth, thus simulating a constant and infinite magma supply.

The models in this paper are produced using Particle Flow Code 6.0 (PFC), commercial software available from Itasca Consulting Group (2017). Particles interact via contact bonds, defined by individual contact models. Previous simulations (Harnett et al., 2018) incorporated parallel bonds for the fluid core and flat joint bonds for the solid talus. The behaviour of each bond is governed by its normal and shear stiffnesses, as well as its cohesive and tensile strengths. The parallel bonds used for the ductile magma provide fluid behaviour by acting as a 'point-style' contact that does not inhibit rotational resistance. For the ductile portion, we assume a constant viscosity of 10^8 Pa in all models (Harnett et al., 2018); a more complete sensitivity analysis to the micro-properties of the magma material can be found in Husain et al. (2014).

Flat joint bonds are used for the solid upper carapace material in models presented here. Flat joint bonds (Potyondy, 2012; Wu and Xu, 2016) are designed to simulate rock behaviour due to their increased interlock and increased rolling resistance, when compared to the parallel bond. The transition between fluid core material and the solid carapace is outlined in detail by Harnett et al. (2018) and is a unidirectional transition based on the solidus pressure for a given melt composition. Couch et al. (2003) calculated the stress conditions under which a melt approaches a maximum crystal packing content, such that its behaviour can be approximated as a solid. Resultant solidus pressures are estimated to range between 0.1 and 5 MPa, dependent on eruptive temperature (Hale, 2008). In all models presented here, we use a solidus pressure of 0.8 MPa. A solidus pressure of 0.8 MPa, as computed by Harnett et al. (2018), ensures that the core volume fraction is not too large, such that the effects of a two-material solid region can be investigated. Using a solidus pressure to control the fluid-solid transition also limits the model in being able to explore exogenous dome growth for the conditions simulated here, as it is not possible for magma to break through the solid crust and reach the surface and form an exogenous lobe (e.g., Fink et al., 1990).

In the models presented here, there is an additional transition from material in the solid upper carapace to the disaggregated talus (Fig. 1). This transition occurs when the stress on the carapace material exceeds the strength of the contact bonds, and simulates fracturing of the solid dome carapace through dome inflation via material addition to the core (Zorn et al., 2019). This transition is also unidirectional, as it simulates breaking of solid rock into loose blocks, and therefore these blocks can never return to solid carapace material.

We newly incorporate the linear rolling resistance contact model (Ai et al., 2011; Wensrich and Katterfeld, 2012) for all disaggregated talus material. The behaviour of contact bonds with the rolling resistance model is primarily defined by a friction coefficient and, unlike flat joints or parallel bonds, rolling resistance contacts cannot be 'bonded' or 'unbonded', because these contacts do not have an associated cohesive strength. By assigning the linear rolling resistance model to particle contacts, a torque acts on the contact pieces to counteract rolling motion – as the models presented here are two-dimensional, resistance to bending in the model is appropriate, as no twisting is possible. In all models presented here, a rolling resistance friction coefficient of 0.84 is used, corresponding to a friction angle of ~40° (sensitivity to this friction coefficient is discussed briefly in Section 3.2). Although individual particles are not intended to represent grains or rocks, by assigning the rolling resistance contact model to the disaggregated talus region, the material is effectively granular and can behave like a slope of loose blocks.

Fig. 1. Cartoon of an idealised lava dome structure, incorporating 1) a viscous fluid core; 2) a solid upper carapace; and 3) disaggregated talus. Existing models incorporate layers (1) and (2). New models presented here include simulation of different behaviour for each of the three layers.

An important boundary condition in the models represented here exists where dome material meets the underlying topography ('walls' in PFC). At these interfaces, the linear rolling resistance contact model is again incorporated, signifying that this material has a purely frictional relationship with the topography. This means that no cohesive strength exists between the dome material and the topography, but also that material cannot be infinitely pushed along the topography, because its frictional properties resist motion.

As described by Harnett et al. (2018), the dome growth simulated in these models is most akin to endogenous dome growth as we do not implement an explicit mechanism for magma reaching the surface, but rather the dome grows through material supplied to its interior.

2.2. Model calibration

It is possible to calibrate the solid modelled material (with flat joint contacts) in PFC with laboratory-scale samples (Potyondy, 2012; Fig. 2), such that specific larger-scale scenarios can be simulated (e.g., Al-Halbouni et al., 2018; Holohan et al., 2011; Poulsen et al., 2018; Schöpfer et al., 2007). Here, we calibrate the modelled material by simulating uniaxial compressive strength tests (i.e., zero confining pressure), following a well-established modelling procedure in PFC (Potyondy, 2016; Potyondy, 2012). The additional benefit of using uniaxial compressive strengths is the wealth of published laboratory data compared with tensile or triaxial testing. For a full exploration of the range of rock strengths expected in volcanic settings, we refer the reader to Heap and Violay (2021). In order to draw broad conclusions about the effect of rock strength on dome geometries, we do not calibrate to a specific suite of laboratory tests on volcanic rocks from a certain volcano, but rather we consider various 'strength scenarios' based on existing knowledge about volcanic rock strengths and the application of laboratory values to the field scale.

Several studies have shown that laboratory-scale strength values must be upscaled in order to accurately represent field-scale behaviour, due to the effect of large-scale discontinuities that cannot be captured in the laboratory. There are various estimates as to how significant this strength reduction is, with some studies suggesting reductions of up to 96% in volcanic rocks (Heap et al., 2018; Okubo, 2004; Thomas et al., 2004; Walter et al., 2019; Watters et al., 2000). In order to account for the reduction in strength expected when laboratory-scale values are upscaled to be applicable to field outcrops, and for the absence of fractures in these models, we calibrate the PFC material to a range of 'upscaled' dome strengths.
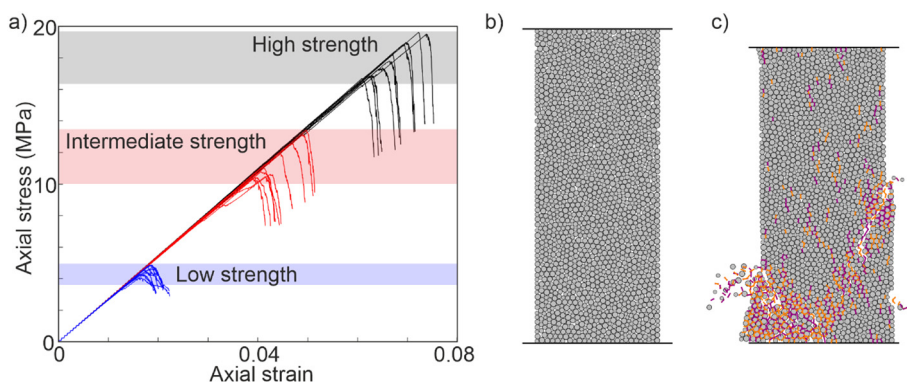
Mechanical strength of volcanic rocks varies with rock type, porosity, permeability, alteration state, and crystal content, among others

(Heap and Violay, 2021, and references therein). In the absence of rock samples for laboratory testing, textural observations such as porosity (Fink and Manley, 1987; Manley and Fink, 1987; Rhodes et al., 2018) can be used to estimate rock strength using pre-established relationships between strength and porosity for volcanic rocks (Heap and Violay, 2021). Laboratory tests show that the uniaxial compressive strengths of dacite varies from 9 to 171 MPa, and for andesite from 2 to 332 MPa (Heap and Violay, 2021), but existing estimates of upscaled dome strength are in the region of 3.7 MPa (Walter et al., 2019) – 6.6 MPa (Heap et al., 2018). For simplicity, and following calibration of the DEM model, we consider three scenarios for dome-scale strength (Fig. 2, Table 1): (1) low strength rock with a UCS value of 4.5 ± 0.3 MPa (blue curves in Fig. 2a); (2) intermediate strength rock with a UCS value of 11.5 ± 1.2 MPa (red curves); and (3) high strength rock with a UCS value of 18.0 ± 1.07 MPa (black curves). These correspond to cohesive bond strengths of 2, 5, and 10 MPa, respectively. In each case, the cohesive to tensile bond strength ratio is maintained at a value of 10, in broad alignment with laboratory tests of tensile strength for volcanic rocks (Harnett et al., 2019a; Heap et al., 2021b; Heap and Violay, 2021; Perras and Diederichs, 2014; Zorn et al., 2018).

An iterative calibration method is required because the absolute values of micro-properties do not equate to the bulk sample properties, i.e., cohesion at the particle-particle scale is not equivalent to the bulk cohesion of a laboratory-scale sample. We follow a well-documented calibration procedure (Potyondy, 2016) which first creates a laboratory-scale (40 × 100 mm) sample in PFC (Fig. 2b), and then performs a uniaxial compression test. For each bond cohesion, we ran multiple numerical experiments with different particle packing arrangements (by defining a different random seed number); this is to simulate natural heterogeneity that would be seen in laboratory testing, and to account for the variation in packing that will exist in the dome-scale models. All other micro-properties are kept constant; a detailed list of these can be found in **Supplementary Material A**. Stress-strain curves from these numerical experiments are shown in Fig. 2a, where curves for bond cohesions of 2, 5, and 10 MPa are blue, red, and black, respectively. The peak axial stress obtained in a given numerical experiment corresponds to its uniaxial compressive strength (UCS). Fig. 2c shows an example of a post-failure sample, showing the macroscopic failure plane (shear cracks shown in magenta, and tensile cracks shown in orange). This sample-scale strength can then be compared with laboratory values.

2.3. Model visualisation

Models are visualised in terms of (1) particle behaviour, i.e., parallel-bonded fluid core (shown as red particles), flat-jointed solid carapace

Fig. 2. (a) Stress-strain curves from repeated laboratory tests in Particle Flow Code (PFC), calibrating the uniaxial compressive strength (UCS) of 40 × 100 mm samples. UCS tests are stopped when the stress reaches 70% of peak stress. For each value of bond cohesion (Table 1), 10 tests are run given a different initial particle packing. For full material parameters, see **Supplementary Material A**. (b) An intact sample generated in PFC, where horizontal lines show walls that enable a compression test to be performed. (c) An example specimen post-failure (i.e., after a compression test), showing crack formation (defined by bond breakage). Shear cracks shown in magenta, and tensile cracks shown in orange. Sample shortening occurs due to strain accommodation.

Table 1

Rock strength scenarios used throughout, as calibrated in Particle Flow Code (PFC).

Rock strength scenario	UCS (MPa)	Bond cohesion in PFC (MPa)
Low	4.5 ± 0.3	2.0
Intermediate	11.5 ± 1.2	5.0
High	18.0 ± 1.07	10.0

Uniaxial compressive strength (UCS) values are an average of ten calibration tests in PFC using different random seed numbers to initiate packing, with an error shown of 1 standard deviation.

(black particles), or disaggregated talus material with the rolling resistance contact model (grey particles); (2) displacement vectors and magnitude; and (3) normalised finite shear strain. Displacement vectors shown throughout calculate average displacements for 40 grid squares that span each dimension of the model domain. The calculation of finite shear strain is described in full by Harnett et al. (2018) but in brief, performs inverse strain modelling by calculating the Cauchy-Green deformation tensor and then computing shear strain (Cardozo and Allmendinger, 2009; Morgan and McGovern, 2005a, 2005b; Schöpfer et al., 2006). This method particularly identifies regions where particles move as coherent blocks of material (i.e., high displacements relative to their neighbours), such that strain localisation can be visualised and located.
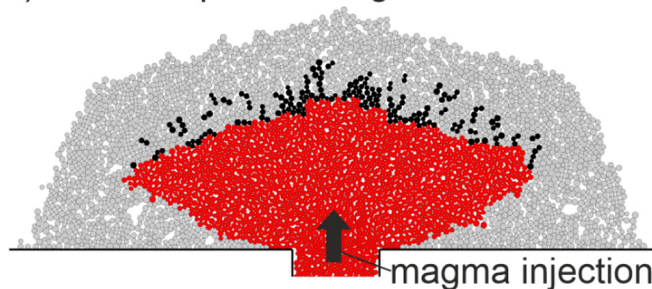
3. Results

3.1. Dome emplacement considering tripartite partitioning

We first examine the effect of rock strength on the relative proportions of solid carapace (shown in black in Fig. 3) and disaggregated talus (shown in grey). In this instance, the 'rock strength' refers to the strength of the flat joint contacts during active emplacement, i.e., the weaker the rock upon transition from fluid to solid, the more easily it disaggregates. We performed three large-scale dome simulations using the three values of UCS determined by our numerical calibration experiments (Fig. 2; Table 1), yielding the following scenarios: (1) the solid fraction of the dome is almost entirely composed of disaggregated talus material when the rock has a low strength (Fig. 3a); (2) the solid fraction of the dome is comprised of an initial solid carapace that borders the core of the dome when the rock has an intermediate strength (Fig. 3b); and (3) there is a significant solid carapace with only a small fraction of disaggregated talus material when the rock has a high strength (Fig. 3c). In each case, disaggregated talus material can be found at the base of the dome (i.e., above the topography but beneath the fluid core, on both sides of the conduit).
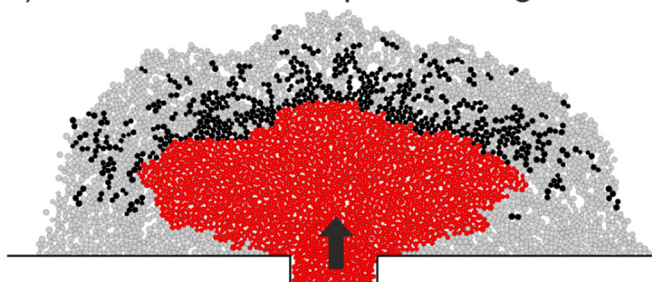
In each scenario, all grown for the same model duration, the proportion of fluid core is approximately equivalent (39–43%). There is a significant effect of rock strength on the ratio of solid to fractured rock, with a low strength rock producing a dome with only 5% solid carapace and 56% disaggregated talus (Fig. 3a), whilst high strength rock results in 41% solid carapace and 16% disaggregated talus (Fig. 3c). The relative proportions of each component remain reasonably consistent through time, with a small increase in core fraction during growth, and a corresponding decrease in solid carapace and disaggregated talus fractions (e.g., at 25% of final growth, the low rock strength model had 25% core, 6% solid carapace, and 69% disaggregated talus; for full evolution see **Supplementary Material B**). These results are similar to findings by Hale et al. (2009b), who showed that the volume of talus undergoing readjustment remained constant as a function of extrusion time.

In the models using intermediate (Fig. 3b) and high rock strength (Fig. 3c), there are several regions where there are small collections of solid carapace particles within a broader region of disaggregated talus. These can be considered as larger solid blocks within slopes of looser blocks; this means they are still able to behave as solid rock but are

Fig. 3. Particle Flow Code (PFC) models of 2D slices of a lava dome, visualising dome material as a function of rock strength, for a solidus pressure of 0.8 MPa. Domes shown have flat joint properties of (a) low rock strength; (b) intermediate rock strength; and (c) high rock strength. Red particles are fluid core material (linear parallel bond contact model), black shows solid upper carapace material (flat joint contact model), and grey shows disaggregated talus material (rolling resistance contact model). Full model properties are listed in **Supplementary Material A**. Quantitative dome volume fractions, and temporal evolution of these during dome growth are provided in **Supplementary Material B**.

not contributing to the maintenance of a solid outer shell. In this respect, we might consider the calculated proportions of disaggregated talus an underestimate in all cases.

3.2. Successive dome emplacement: Horizontal topography

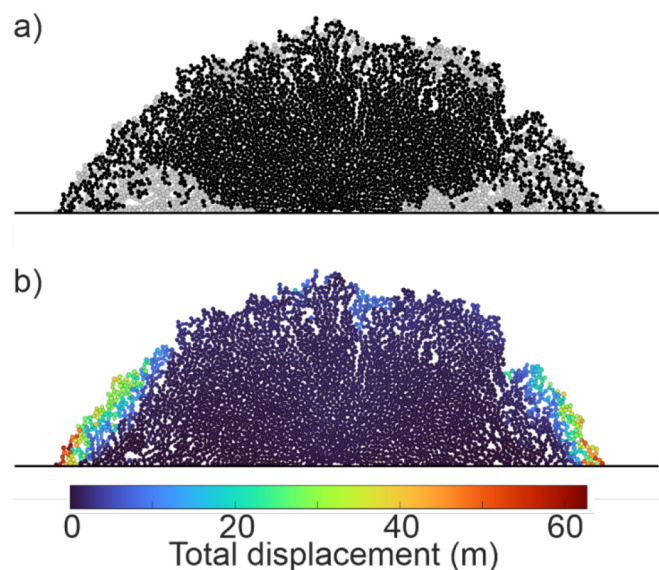The initial dome emplacement shown in Fig. 3a-c produces a dome with a mostly flat top, and over-steepened slopes. This is similar to both field observations (Bull et al., 2013; Darmawan et al., 2018; Hutchison et al., 2013; Rosas-Carbajal et al., 2017; Zorn et al., 2020b) and analogue experiments (Závada et al., 2009; Zorn et al., 2020a). Once extrusion slows or ceases, it is expected that domes continue to

settle due to the effect of gravity, likely through processes of lateral spreading and dynamic spalling of material on oversteepened slopes (e.g., Major et al., 2009). This settling can cause pronounced effects on the overall morphology, and likely occurs due to relaxation after internal pressures decrease once effusion ends (Bull et al., 2013). For example, the top of the February 1981 lobe at Mt. St Helens (Washington, USA) was seen to subside by ~8 m due to settling during a pause in extrusion (Swanson et al., 1987). We consider this process to be similar to simple volcano spreading mechanisms, with the fluid core acting as an internal weakness and allowing slow outward deformation. This spreading mechanism has been observed in existing numerical models (e.g., Heap et al., 2021), analogue models (e.g., Cecchi et al., 2004; van Wyk de Vries et al., 2000), and field observations (e.g., van Wyk de Vries and Francis, 1997).

To simulate the effects of successive dome extrusion, a dome (Dome 1) is first emplaced onto simplified horizontal topography and then the addition of new material is stopped, and the dome is allowed to settle under gravity until the dome is quasi-stable. During simulation of this process, the core also undergoes complete solidification. A limitation of the current model is that this solidification is artificially instant, when in reality it likely occurs over much longer timescales on the order of months to years (e.g., Ball et al., 2015). In the model shown here, strong rock was simulated (Table 1) both during initial emplacement and during solidification prior to settling.

Fig. 4 shows the effects of solidification of the fluid core and gravitational settling on dome morphology – in this case, the dome is settled until it reaches quasi-equilibrium. The settling process primarily occurs through readjustment of the talus material, where material on the oversteepened slopes disaggregates and tends towards the material's angle of friction. The post-settling dome is therefore considered 'stable', as it does not displace without the introduction of additional perturbing factors. This settling is sensitive to the friction coefficient assigned to the rolling resistance contacts, in that a lower friction coefficient leads to shallower dome flanks (**Supplementary Material C**).

This is only observed after settling and does not significantly affect newly emplaced domes, as their upward force (e.g., from ascent velocity, magmatic pressure) exceeds the downward gravitational force controlling talus readjustment.

A second dome (Dome 2) is then extruded. Dome 2 is extruded with the same properties as Dome 1, with the new conduit translated to the right of Dome 1. The idea that this type of shift in a conduit's position can occur has been discussed by previous authors (Le Corvec et al., 2018; Maccaferri et al., 2017; Zorn et al., 2019), where either the addition of dome material or the significant excavation of material exerts control on the dynamics of the shallow conduit system due to the local changes in stress field. Similar effects on conduit morphology could be caused by formation of a dense plug at the top of the conduit during periods of slow or no extrusion. The formation of a dense plug can cause deflection of incoming lava oblique to the prior pathway to the surface (Hale and Wadge, 2008; Husain et al., 2014; Lavallée et al., 2012; Watts et al., 2002; Zorn et al., 2019). For simplicity, no subsurface magmatic architecture is reproduced in these models, but rather the vent is relocated.

In the two-dome simulation, Dome 1 acts as a buttress for the growth of Dome 2, with the morphology of Dome 2 otherwise similar to the uninhibited growth of Dome 1 (Fig. 5). As the stress calculation is driven by the vertical overburden of material in this model, there is likely an underestimation of solid carapace/disaggregated talus material to the left of Dome 2. Assuming Dome 1 has undergone cooling at the surface, there would likely be a thin contact region of solidification in Dome 2 that is not simulated here.

Growth of Dome 2 causes lateral displacement of the previously stable Dome 1, with displacements on the right flank of up to 5 m (Fig. 5c). Visualising the accumulation of strain within the dome (Fig. 5b) shows significant strain accumulation in both the solid carapace and disaggregated talus to the right of the dome (i.e., the area of highest displacement). Accumulation of strain is also seen towards the centre of the dome. There does not appear to be any formation of deep-seated failure
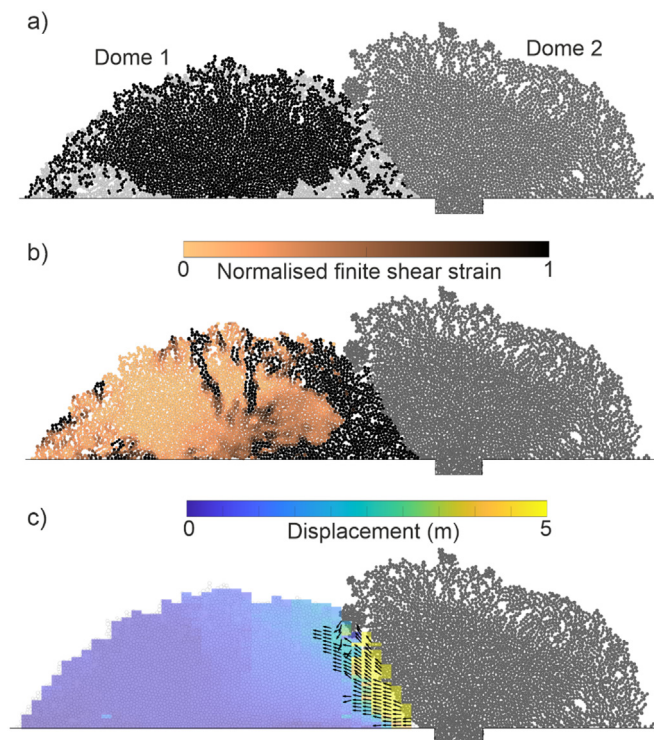

Fig. 4. Particle Flow Code (PFC) models of 2D slices of a lava dome, showing a dome emplaced onto horizontal topography following a period of no extrusion, solidification, and settling. Panel (a) shows material properties, where black is solid carapace (and artificially solidified core material), while grey shows disaggregated talus. Panel (b) shows the same model result as a function of total displacement since extrusion was ceased.

Fig. 5. Particle Flow Code (PFC) models of 2D slices of a lava dome, considering destabilisation of previously stable Dome 1 after emplacement of Dome 2. (a) Solid upper carapace material shown in black, including artificially solidified core material, with disaggregated talus shown in light grey. (b) Normalised finite shear strain in Dome 1, where darker areas show higher strain accumulation. (c) Displacement of Dome 1, where colour indicates magnitude and arrows indicate direction only. Dome 2 shown in dark grey for reference in all panels.

planes (e.g., Harnett et al., 2018), however the strain distribution suggests formation of fracture-type features that are approximately radial (Fig. 5c). It is possible that these fractures form due to the higher proportion of solid carapace material directly above the conduit compared to the higher proportion of disaggregated material on the dome slopes (Fig. 5a), such that the solid rock is more resistant to the force exerted by the growth of Dome 2.

3.3. Successive dome emplacement: Sloped topography

We present a similar suite of models for the emplacement of two successive domes onto a topographic slope of 20°. We consider this to be a more hazardous starting condition for dome growth, according to both observations (Calder et al., 2002; Walter et al., 2013) and numerical models (Harnett et al., 2018) that show increased displacement and strain accumulation on downhill dome flanks. Although we show here a suite of models where magma is extruded onto a 20° slope, we suggest that steeper slopes (possible in some volcanic settings) could promote more significant instabilities and therefore larger collapse volumes.

Emplacement of Dome 1 onto a 20° slope shows an oversteepened downhill dome flank (Fig. 6a) as seen under the same conditions modelled by Harnett et al. (2018). Settling and solidification of Dome 1 (given strong rock properties) produce a complex dome morphology that has a lobe-like feature on its downhill flank (Fig. 6b) due to displacement of the previously oversteepened portion (Fig. 6c). This is reasonably consistent with topographic profiles from existing domes

Fig. 6. Particle Flow Code (PFC) models of 2D slices of a lava dome showing emplacement of a dome onto sloped topography. (a) Emplacement of a dome onto a 20° slope, where red shows fluid viscous core, black shows solid upper carapace, and grey shows disaggregated talus material. (b) Dome 1 after settling and solidification of core material, colours as in (a). (c) The same model scenario as panel (b), showing displacement during the settling period.
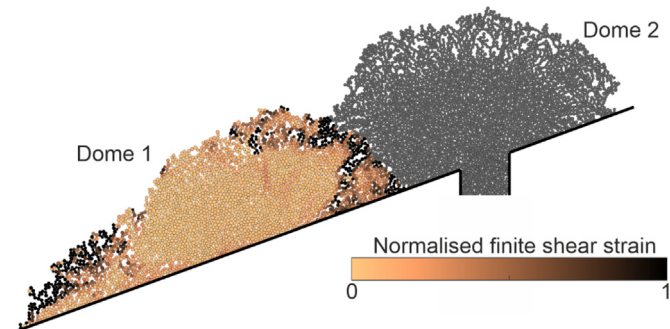
emplaced onto sloped topography (e.g., Diefenbach et al., 2013), where observed domes shallow towards their tail. Dome 1 is again settled until it reaches a quasi-stable state, where further deformation cannot occur without the addition of external perturbation factors.

The addition of a second dome (Dome 2), extruded upslope from Dome 1, in this scenario leads to strain accumulation and displacement downhill in Dome 1 (Figs. 7, 8a). As expected, the bulk of this displacement occurs near to the zone of contact between the two domes, with additional displacement occurring on the downhill flank in the form of talus readjustment (Fig. 8a). We consider this talus readjustment to be similar to the accommodation of extension discussed by Hutchison et al. (2013), who observed lateral lava dome advancement by rockfall events at the dome edges (see also Darmawan et al., 2020; Mueller et al., 2013). Visualising the internal strain shows a potential plane of detachment where the underlying disaggregated material meets the core (Fig. 7). In this scenario, the presence of disaggregated talus further destabilises the dome, highlighting that full consideration of lava dome models must include both the solid carapace as well as the disaggregated talus material in order to accurately capture their behaviour.
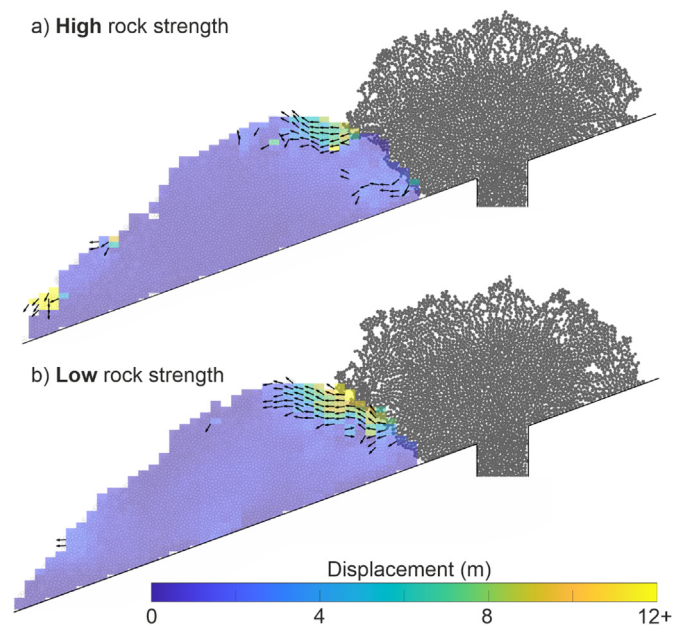
3.4. Successive dome emplacement following alteration

The same successive dome emplacement scenario can be considered for a weaker rock strength, assuming that during a period of no extrusion and settling, progressive weakening of the rock occurred. Such weakening following emplacement can occur through extensive hydrothermal alteration (Ball et al., 2015; del Potro and Hürlimann, 2009; Farquharson et al., 2019; Heap et al., 2019; Heap et al., 2015; Kereszturi et al., 2020; Mordensky et al., 2019; Wyering et al., 2014). Although we acknowledge that hydrothermal alteration can result in rock strengthening (Heap et al., 2021a), we explicitly model here the scenario in which alteration reduces rock strength. Fig. 8 shows the displacement of Dome 1 following the emplacement of Dome 2 for a high-strength Dome 1 (Fig. 8a, discussed in the previous section) and a low-strength or hydrothermally altered Dome 1 (Fig. 8b). The weaker dome (Fig. 8b), shows more significant lateral displacement, with 74% of material displacing over 1 m, compared with only 52% of material in the high strength dome (Fig. 8a).

Both low- and high-strength domes show displacement focussed on the contact region of Domes 1 and 2 (Fig. 8). The stronger dome shows a greater degree of displacement on the downhill slope; this is because the higher proportion of disaggregated talus in the weaker dome led to a shallower slope after settling. As a result, the additional forces exerted on Dome 1 by the emplacement of Dome 2 cause less significant further displacement of the shallow downhill slope in the weaker dome (Fig. 8b). Destabilisation and readjustment of the downhill slope is, however, observed in the scenario with strong rock (Fig. 8a).

Fig. 7. Particle Flow Code (PFC) models of 2D slices of a lava dome, visualised in terms of normalised finite shear strain in Dome 1, following emplacement of Dome 2. Before emplacement of Dome 2, Dome 1 was settled and stable. A detachment plane can be seen at the right edge of Dome 1 - refer to Fig. 6 to see distribution of solid carapace and disaggregated talus material in Dome 1.

Fig. 8. Comparison of displacement in Dome 1 given (a) high rock strength, and (b) low rock strength. In each case, Dome 1 was extruded onto a topographic slope of 20°, settled and solidified until stable, and then Dome 2 was extruded. Velocity vectors show direction of movement only, while colours indicate magnitude of displacement. Dome 2 shown in grey for reference only in each case.

The detachment plane is also less visible in the weak rock scenario. In the weaker dome, there is a less significant material contrast between solid carapace material and disaggregated talus material due to the higher proportion of material that disaggregated during initial growth of Dome 1 (Fig. 8b). In the stronger dome, the downhill dip of the material contrast acts as a pre-existing plane of weakness and facilitates high strain accumulation.

Although higher total displacement is seen in the weaker dome, the emergence of the deep detachment plane in the stronger dome may suggest large-scale instability over longer timescales. These data therefore suggest that geometric effects and existing material heterogeneity can significantly affect dome stability, such that stronger dome rock does not necessarily signify a more stable dome.

3.5. Crater wall instability due to dome growth

Lava domes are commonly emplaced within a crater and can grow to fill the crater (Macías and Siebe, 2005) or overtop the crater walls and form rockfalls and pyroclastic density currents that flow downslope (Herd et al., 2005; Mueller et al., 2013; Wadge et al., 2008; Walter et al., 2019). Crater walls themselves are therefore key in determining the morphology, size, and stability of a lava dome. Indeed, recent observations at Merapi (Indonesia) suggest than even small changes in summit morphology can control dome growth and evolution (Kelfoun et al., 2021). Specific dome collapses have been attributed to mechanical weakening and structural failures of crater walls, including two collapses at Volcan de Colima in July 2015 (Lesage et al., 2018) and the Boxing Day collapse at Soufriere Hills Volcano in 1997 (Voight et al., 2002; discussed in more detail later).

As a result of this importance, we also provide simulations in which we emplaced domes inside a crater (Fig. 9). This was previously done by Harnett et al. (2018) but, in our new simulations, we construct the topography using a particle-based method, instead of using simple walls in PFC (Fig. 9a). This allows for the investigation of the stability of the crater walls themselves. We use a symmetric crater geometry, but position the conduit off-centre to allow for comparison of one crater wall which is subjected to increased loading due to dome growth, and one crater wall which is not (Fig. 9a).

We present here two end member models: (1) a crater with strong rock properties (bond cohesion = 10 MPa; Fig. 9b), and (2) a crater with weak rock properties (bond cohesion = 2 MPa; Fig. 9c). We increase the Young's modulus of the material to account for the 2D nature of the cross section, such that the crater can be gravitationally stable before dome growth begins. In each scenario, a dome is emplaced with strong rock properties (Table 1).

The stronger crater material (Fig. 9b) shows displacements on the order of 1 m at the apex of the crater wall, with a dominant lateral sense of motion (i.e., the dome is pushing the crater wall outwards). In the scenario with weaker crater material (Fig. 9c), the magnitude of displacement is broadly similar, but there is a much larger region of displacement. The dominant sense of motion is downward and outward, suggesting this scenario lends itself more to landslide generation (Hungr et al., 2014). Visualising strain in each case does not show deep-seated failure planes, suggesting that the crater wall material is not moving as one coherent block. This is likely because the material is sufficiently weak to break up as it is pushed downslope by the lateral forces of the growing dome. These scenarios show that weakening of existing topographic structures, by hydrothermal alteration or other mechanisms, can significantly impact stability of the volcanic system, as displacement of the crater wall would destabilise the dome flank and could lead to retrogressive collapse.

The models in Fig. 9 show that a growing dome can destabilise a triangular wedge of material, that in this case corresponds to the pre-existing crater wall. We suggest also that such a conclusion can be extended: if a buttressing wedge of talus from earlier eruptive phases is weakened, a growing dome could equally cause displacement of this material wedge. This may facilitate additional flow front advancement or generate small-scale downslope instabilities that eventually lead to retrogressive collapse. It is therefore important to consider the nature of pre-existing substrate in overall assessment of volcanic stability, whether this be a crater wall or older talus material.
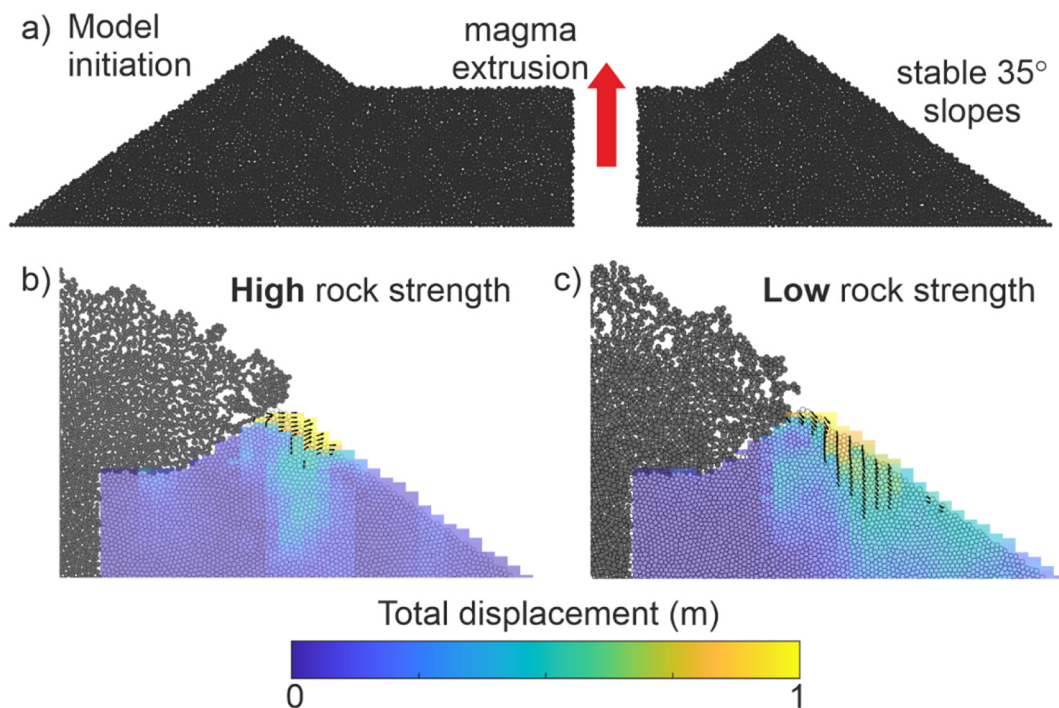
4. Discussion

4.1. Talus behaviour

The nomenclature surrounding the solid portion of lava domes is poorly defined, and the term 'talus' is commonly used in the literature to refer to all solid portions of a dome. Although lava domes have long been conceptually understood to have a solid carapace and a more frictionally-controlled talus, distinct material behaviour of these regions has not been incorporated into previous numerical models (Hale et al., 2009a, 2009b; Harnett et al., 2018).

Hale et al. (2009b) discussed how it can be tempting to consider talus behaviour as similar to a sandpile, where the material tends to its angle of repose and exhibits self-organised criticality (Bak et al., 1988). Nagel (1992) suggested that sandpiles in fact have two important angles governing stability: one that exists prior to avalanche, and one smaller angle that exists immediately after. One could argue that this is somewhat similar to the talus morphology discussed by Pérez (1998), who assessed transects of talus slopes at Chaos Crags (Lassen volcanic center, California, USA) and determined a bi-segmented slope profile, with a steeper upper segment where the slope angle is ~37° (i.e., a slope prior to avalanche), followed by a somewhat abrupt break in slope near the base where the angle dropped to <7° (i.e., post-avalanche). However, talus slopes also differ from simple sandpile experiments, in that they include grains of different sizes (in the form of larger boulders) that can themselves disaggregate downslope.

The method proposed here allows for the incorporation of the sandpile-like aspects of a talus slope - through the rolling resistance model acting in the disaggregated talus - whilst still allowing for larger grain sizes to disaggregate downslope, through flat-jointed solid carapace material within a matrix of disaggregated talus. The result is a more complex lava dome morphology (Fig. 3) than that suggested by

Fig. 9. Particle Flow Code (PFC) models of a cratered scenario. (a) Model initiation showing construction of a gravitationally stable cratered scenario with 35 degree slopes. (b) Displacement of the crater walls due to dome growth. Crater walls assigned high rock strength. (c) Displacement of the crater walls due to dome growth. Crater walls assigned low rock strength. Arrows show direction of motion in each case, whilst colours indicate magnitude.

idealised cross sections of rhyolite flows (Christiansen and Lipman, 1966; Duffield and Dalrymple, 1990), dome flow fronts (Huppert et al., 1982), and finite element method lava dome cross sections (Hale et al., 2009b; Hale et al., 2009a; Hale et al., 2007). The more complex morphology could relate also to observation timescale: domes may be more readily observed late in their growth, meaning that more of the solid carapace has disaggregated to form talus due to lateral spreading (e.g., Hutchison et al., 2013).

At a growing dome, the formation of disaggregated talus releases heat and gases from the dome interior. The consideration of both a solid outer shell *and* disaggregated talus slopes is key to obtaining a more holistic understanding of a lava dome's morphology. Wadge et al. (2009) suggest that a lava dome that has already converted more of its mass to a clastic component is potentially less hazardous than one retaining a higher proportion of its mass in its core. This suggestion was broadly supported by Harnett et al. (2018), where wholesale collapse was only made possible by the formation of deep-seated failure planes that involved core material (and therefore released energy stored in the core following rapid decompression, a process shown to increase pyroclastic flow velocity and therefore increase hazard potential (Fink and Kieffer, 1993)). Incorporation of both the carapace and talus slopes within this model allows for a more detailed investigation of dome stability by considering a more complex internal structure in the modelled scenarios.

The models shown here (e.g., Fig. 7) demonstrate the importance of modelling the distinction between solid carapace and disaggregated talus, as this can be key in pre-defining planes of weakness within the dome shell, and therefore acting as sliding planes for overriding dome material.

4.2. Loading effects of successive dome emplacement

Sequential lava dome emplacement and destruction has been observed at several volcanoes worldwide (e.g., Matthews et al., 1997; Mendoza-Rosas et al., 2017; Rhodes et al., 2018). Domes can be removed by explosive activity, but on several occasions, conduit relocation leads to successive domes being emplaced within the same crater or collapse scar, such as during the 2004–2008 eruption at Mt. St Helens (Dzurisin et al., 2015; Ryan et al., 2018), during the last century of dome-forming eruptions at Merapi volcano (Voight et al., 2000), during the emplacement of the dome complex at Chaos Crags (Clynne and Muffler, 2017), and during the 2021 eruption of La Soufrière in Saint Vincent and the Grenadines (Eastern Caribbean). We have demonstrated here that sequential dome extrusion can destabilise otherwise stable domes by exerting additional lateral forces and oversteepening slopes (Figs. 5, 7). We show that this primarily results in rockfalls and avalanches from the oversteepened slopes and is unlikely to preclude deeper-seated failures.

A good example of a complex centre of multiple domes/lobes is Chaos Crags, a centre consisting of six rhyodacitic domes (named Domes A to F in chronological order of emplacement). These domes represent the youngest eruption in the Eagle Peak sequence (Clynne et al., 2008) and are part of the Lassen volcanic center in California, USA (Clynne and Muffler, 2017; Ryan et al., 2020). The majority of Dome C collapsed approximately 350 years ago (Clynne and Muffler, 2017), leaving a semi-spherical collapse scar and a large avalanche deposit called Chaos Jumbles that extends NW of the remnants of Dome C. The cause of the rock avalanche generating instability of Dome C is to date unknown, although several mechanisms have been proposed. These include an explosion at the base of the dome, renewed activity at neighbouring Dome D, and a large earthquake originating from the Hat Creek Fault (Clynne and Muffler, 2017). Although we do not aim to forward a definitive mode of failure of Dome C, we note this as a prime example where renewed dome emplacement may have contributed to destabilisation of an existing dome.

Dome D was reported to be emitting steam and other gases during the period of 1854–57 (Clynne and Muffler, 2017; Williams, 1932), suggesting possible activity or dome growth. Dome D is seen to adjoin older domes from which rockfalls originated during the same time period, i.e., Dome C. Crandell et al. (1974) suggested that the growth of a new

dome within the central part of an older dome group may have caused oversteepened slopes, and subsequent rockfall generation, due to pushing and tilting of surrounding rocks (i.e. exertion of a large lateral force). Crandell et al. (1974) note that this oversteepening is more likely to result in rockfalls if the rocks are highly fractured, or altered (as documented by Heap et al., 2021a), as we demonstrate in the modelled sloped scenario (Fig. 8). The models in this contribution therefore act as a proof of concept and allow for more specific scenarios to be simulated and potential modes of failure to be determined.

4.3. Rock strength effects on dome stability

Our results show the effect of rock strength on dome stability in two distinct ways: (1) the role of rock strength in determining the relative proportions of solid carapace to disaggregated talus (Fig. 3); and (2) the role of low rock strength (e.g., due to hydrothermal alteration) in destabilising emplaced dome flanks (Figs. 8, 9). Both mechanisms have significant hazard implications, which we discuss here.

Conclusions from Harnett et al. (2018) showed that talus volumes significantly influence the accumulation of shear strain within a dome, and consequently play a key role in determining the potential dome volumes that might be subject to collapse. We have shown here that rock strength, determined primarily by melt crystallinity and porosity due to gas exsolution, is one factor that affects the ratio of solid carapace to disaggregated talus. We suggest the ratio of these materials, a function of rock strength, is key in defining overall dome stability. We note that this ratio is likely also affected by extrusion rate, a factor not considered in the models presented here. We therefore suggest that the strength of rock samples collected from new or developing domes should be tested in the laboratory, to provide important information on the potential hazards posed by a particular dome.

The spreading of the lava dome core on top of a solid layer, as opposed to directly contacting the free-surface of the volcano crater, has been observed in previous numerical models (Hale, 2008; Harnett et al., 2018). Significant hazard implications have been discussed as a consequence of this geometry, as this region may be more subject to erosion or penetration via rainfall due to talus readjustment/avalanches. Removal of this talus can undermine the mechanical strength of the apron and therefore leave the unbuttressed core to breakout and form (as seen at Volcán de Colima (Mexico) in 2009; Hutchison et al., 2013) or to collapse completely. Alternately, exposure of the hot fluid core due to talus removal can lead to rapid decompression and explosive activity (Alidibirov and Dingwell, 1996; Robertson et al., 1998; Voight and Elsworth, 2000).

Despite the hazard implications of this buttressing material, previous models have not distinguished between the intact and disaggregated solid portions of the outer dome shell. We show here than even in the high rock strength scenario, the material underlying the core is predominantly disaggregated talus (Fig. 3). We therefore suggest that the hazard presented by this material contrast exists even in domes that appear to have a coherent outer shell and high crystallinity lavas.

We have also demonstrated here that a lower rock strength results in higher total displacement (Fig. 8), where the unstable material volume (where displacements >1 m) is approximately 50% higher than in simulations with high rock strength. In addition to the higher displacements we show here, a previous study by Eppler et al. (1987) suggested that the thicknesses and runouts of rockfall avalanches at Chaos Crags were strength-dependent, such that a lower strength could produce more significant deposit volumes. Ball et al. (2018) also found, using a 3D numerical model, that collapse volume increased as a function of increasing alteration-induced weakening.

The difference in displacement pattern with rock strength is particularly pertinent when considering the cratered dome growth scenario, as lower rock strength leads to downward and outward movement as opposed to purely outward movement (Fig. 9), suggesting possible development of a deep rotational failure instead of a lower volume topple. This

scenario was observed at the Soufrière Hills dome in Montserrat where weakening at the base of the retaining crater wall (Galway's wall) was a major contributing factor in the destabilisation and collapse of the lava dome on 26 December 1997 (Sparks et al., 2002; Voight et al., 2002), particularly when coupled with loading from the static weight of dome rock as well as dynamic loading from shallow hybrid earthquakes (Young et al., 2002). The crater walls are arguably more susceptible to weakening than the dome itself; indeed Galway's wall was comprised of highly fragmental material from cemented pyroclastic flow deposits and tephra layers and was located ~500 m North of an active hot spring area with strongly hydrothermally altered rocks (Young et al., 2002). The Boxing Day event produced a large debris avalanche with a ~ 4 km runout (Woods et al., 2002), destroying two villages on the southwestern coast of Montserrat and resulting in a small tsunami (Young et al., 2002). The wall was further destabilised by face-parallel and radial cracks; we do not simulate the additional destabilising effect of fractures in the models presented here, suggesting that we could be overestimating stability. Instability was likely also promoted by the steep 50° angle of the outward dipping crater wall face (Young et al., 2002).

The collapse of Soufrière Hills was followed by a lateral blast as the lava dome core was exposed (Woods et al., 2002; Young et al., 2002). The mechanical instability of the dome was a direct consequence of the crater wall weakening, but one could also argue that this weakening ultimately led to a change in eruption dynamics, as the unloading of the system may have contributed to the pause in extrusion in March 1998. Our analysis concurs with that made by Young et al. (2002), who stated that sector collapse may represent the most severe volcanic hazard during andesitic dome-forming eruptions, as we find the displacement patterns are distinctly different for differing rock strengths (Fig. 9), and expect the hazard implications of this to be greater than for dome flank displacement (Fig. 8).

In this pilot study of calibrating rock properties in lava dome emplacement models, we do not consider spatial or temporal variation. Spatial distribution of rock strength is key to consider in future models, particularly when considering a volcano subject to hydrothermal alteration (e.g., Heap et al., 2021a). Cooling and solidification processes are also not simulated here. Cooling, for example, can create thermal cracks (Browning et al., 2016; Lamur et al., 2018) that could reduce rock strength. Heap et al. (2018) also showed, using high-temperature uniaxial deformation experiments, that a reduction in temperature could reduce the strength of andesite, due to the re-opening of microcracks as a result of thermal contraction. Similar conclusions were drawn by Coats et al. (2018). The influence of temperature fluctuations on the mechanical behaviour and strength of volcanic rock is likely further complicated by the presence of clays and/or zeolites (Heap et al., 2012; Weaver et al., 2020). These spatial and temporal variations in rock strength are not currently incorporated into DEM models but are an avenue to be pursued in future modelling efforts.

5. Conclusions

In this study, we used the discrete element method to computationally model lava dome growth, considering a ductile fluid core, a solid upper carapace, and a disaggregated talus portion. We calibrated the solid portion of the dome to three different rock strength scenarios (micro-cohesion values of 2, 5, and 10 MPa), and show the effect of varied rock strength on dome deformation given successive dome emplacement, and crater wall weakening. From our simulations, we conclude the following:

(1) When considering dome structure, it is crucial to include distinct material properties and behaviour for solid dome rock and disaggregated talus material. Rock strength is one factor that determines the relative proportions of these components.
(2) The presence of disaggregated talus at the base of a dome can act as a pre-existing sliding plane, particularly when it is overlain by

intact dome rock. This plane of material contrast is more likely to occur in a dome with more crystalline, stronger rock.

(3) Sequential lava dome emplacement can lead to destabilisation of a previously emplaced dome, even if this dome was quasi-stable prior to the growth of the new dome. This is more pronounced on a sloped topography, but also occurs on horizontal topography.

(4) Lower rock strength (e.g., resulting from hydrothermal alteration) leads to higher unstable material volumes in domes. This is particularly key when considering the properties of crater walls, as homogenous lower rock strength promotes deeper-seated failure.

We suggest that, where possible, strength analysis of dome material is key for understanding its stability profile, as well as the production of digital elevation models to allow real-time volcano-specific modelling to be performed. Where approaching a dome for sample collection is too hazardous, we suggest monitoring of the following: 1) evidence of hydrothermal alteration at the surface (e.g. discoloration) to infer the location of fluid pathways and potential strength changes in surrounding rocks; 2) displacement and/or deformation of existing domes where there is new adjacent lobe emplacement; and 3) high temporal resolution imagery that allows assessment of disaggregation of material during dome growth, such that it might be possible to estimate the proportion of disaggregated talus. We consider the real-time integration of numerical models and observations key to reducing hazard potential.

Author statement

CH was responsible for conceptualization, methodology, software, formal analysis and writing of the manuscript. MH was responsible for conceptualization, design of methodology, and writing of the manuscript. Both CH and MH were responsible for funding acquisition.

Declaration of interests

The authors declare that they have no known competing financial interests or personal relationships that could have appeared to influence the work reported in this paper.

Declaration of Competing Interest

None.

Acknowledgements

Appendix A. Supplementary data

Supplementary data to this article can be found online at https://doi.org/10.1016/j.jvolgeores.2021.107398.

References

Ai, J., Chen, J., Rotter, J.M., Ooi, J.Y., 2011. Assessment of rolling resistance models in discrete element simulations. Powder Technol. 206, 269–282. https://doi.org/10.1016/j.powtec.2010.09.030.

Al-Halbouni, D., Holohan, P.E., Taheri, A., Schöpfer, M.P.J., Emam, S., Dahm, T., 2018. Geomechanical modelling of sinkhole development using distinct elements: Model verification for a single void space and application to the Dead Sea area. Solid Earth 9, 1341–1373. https://doi.org/10.5194/se-9-1341-2018.

Alidibirov, M., Dingwell, D.B., 1996. Magma fragmentation by rapid decompression. Nature. https://doi.org/10.1038/380146a0.

Bak, P., Tang, C., Wiesenfeld, K., 1988. Self-organized criticality. Phys. Rev. A 38, 364–374. https://doi.org/10.1103/PhysRevA.38.364.

Ball, J.L, Stauffer, P.H., Calder, E.S., Valentine, G.A., 2015. The hydrothermal alteration of cooling lava domes. Bull. Volcanol. 77, 102. https://doi.org/10.1007/s00445-015-0986-z.

Ball, J.L, Taron, J., Reid, M.E., Hurwitz, S., Finn, C, Bedrosian, P., 2018. Combining multiphase groundwater flow and slope stability models to assess Stratovolcano Flank Collapse in the Cascade Range. J. Geophys. Res. Solid Earth 123, 2787–2805. https://doi.org/10.1002/2017JB015156.

Blake, S., 1990. Viscoplastic Models of Lava Domes, in: Lava Flows and Domes: Emplacement Mechanisms and Hazard Implications. Springer Berlin Heidelberg, Berlin, Heidelberg, pp. 88–126 https://doi.org/10.1007/978-3-642-74379-5_5.

Bourgouin, L., Hale, A.J., Arsac, A., 2007. Studying the influence of a solid shell on lava dome growth and evolution using the level set method. Geophys. J. Int. 170, 1431–1438. https://doi.org/10.1111/j.1365-246X.2007.03471.x.

Browning, J., Meredith, P., Gudmundsson, A., 2016. Cooling-dominated cracking in thermally stressed volcanic rocks. Geophys. Res. Lett. 43, 8417–8425. https://doi.org/10.1002/2016GL070532.

Bull, K.F., Anderson, S.W., Diefenbach, A.K., Wessels, R.L., Henton, S.M., 2013. Emplacement of the final lava dome of the 2009 eruption of Redoubt Volcano, Alaska. J. Volcanol. Geotherm. Res. 259, 334–348. https://doi.org/10.1016/j.jvolgeores.2012.06.014.

Byrdina, S., Friedel, S., Vandemeulebrouck, J., Budi-Santoso, A., Suhari, Suryanto, W., Rizal, M.H., Winata, E., Kusdaryanto, 2017. Geophysical image of the hydrothermal system of Merapi volcano. J. Volcanol. Geotherm. Res. 329, 30–40. https://doi.org/10.1016/j.jvolgeores.2016.11.011.

Calder, E.S., Luckett, R., Sparks, R.S.J., Voight, B., 2002. Mechanisms of lava dome instability and generation of rockfalls and pyroclastic flows at Soufrière Hills Volcano, Montserrat. Geol. Soc. Lond. Mem. 21, 173–190. https://doi.org/10.1144/GSL.MEM.2002.021.01.08.

Calder, E.S., Lavallée, Y., Kendrick, J.E., Bernstein, M., 2015. Lava Dome eruptions. Encycl. Volcanoes, 343–362 https://doi.org/10.1016/b978-0-12-385938-9.00018-3.

Cardozo, N., Allmendinger, R.W., 2009. SSPX: a program to compute strain from displacement/velocity data. Comput. Geosci. 35, 1343–1357. https://doi.org/10.1016/j.cageo.2008.05.008.

Cecchi, E., van Wyk de Vries, B., Lavest, J.M., 2004. Flank spreading and collapse of weak-cored volcanoes. Bull. Volcanol. 67, 72–91. https://doi.org/10.1007/s00445-004-0369-3.

Christiansen, R.L., Lipman, P.W., 1966. Emplacement and thermal history of a rhyolite flow near Fortymile Canyon, Southern Nevada. Geol. Soc. Am. Bull. 77, 671–684. https://doi.org/10.1130/0016-7606(1966)77[671:EATHOA]2.0.CO;2.

Clynne, M.A., Muffler, L.J.P., 2017. Geologic field-trip guide to the Lassen segment of the Cascades Arc, northern California. US Geol. Surv. Sci. Investig. Rep. https://doi.org/10.3133/sir20175022K2.

Clynne, M.A., Christiansen, R.L., Trimble, D.A., Mcgeehin, J.P., 2008. Radiocarbon Dates from Volcanic Deposits of the Chaos Crags and Cinder Cone Eruptive Sequences and Other Deposits, Lassen Volcanic National Park and Vicinity, California.

Coats, R., Kendrick, J.E., Wallace, P.A., Miwa, T., Hornby, A.J., Ashworth, J.D., Matsushima, T., Lavallée, Y., 2018. Failure criteria for porous dome rocks and lavas: A study of Mt. Unzen, Japan. Solid Earth 9, 1299–1328. https://doi.org/10.5194/se-9-1299-2018.

Collinson, A.S.D., Neuberg, J.W., 2012. Gas storage, transport and pressure changes in an evolving permeable volcanic edifice. J. Volcanol. Geotherm. Res. 243–244, 1–13. https://doi.org/10.1016/j.jvolgeores.2012.06.027.

Couch, S., Harford, C.L., Sparks, R.S.J., Carroll, M.R., 2003. Experimental constraints on the conditions of formation of highly Calcic Plagioclase Microlites at the Soufrière Hills Volcano, Montserrat. J. Petrol. 44, 1455–1475. https://doi.org/10.1093/petrology/44.8.1455.

Crandell, D.R., Mullineaux, D.R., Sigafoos, R.S., Rubin, M., 1974. Chaos crags eruptions and Rockfall-avalanches, Lassen Volcanic National Park, California. J. Res. US. Geol. Surv. 2, 49–59.

Darmawan, H., Walter, T.R., Brotopuspito, K.S., Subandriyo, I Gusti Made Agung Nandaka, 2018. Morphological and structural changes at the Merapi lava dome monitored in 2012–15 using unmanned aerial vehicles (UAVs). J. Volcanol. Geotherm. Res. 349, 256–267. https://doi.org/10.1016/j.jvolgeores.2017.11.006.

Darmawan, H., Yuliantoro, P., Rakhman, A., Budi Santoso, A., Humaida, H., Suryanto, W., 2020. Dynamic velocity and seismic characteristics of gravitational rockfalls at the Merapi lava dome. J. Volcanol. Geotherm. Res. 404. https://doi.org/10.1016/j.jvolgeores.2020.107010.

del Potro, R., Hürlimann, M., 2009. The decrease in the shear strength of volcanic materials with argillic hydrothermal alteration, insights from the summit region of Teide stratovolcano, Tenerife. Eng. Geol. 104, 135–143. https://doi.org/10.1016/j.enggeo.2008.09.005.

Diefenbach, A.K., Bull, K.F., Wessels, R.L., McGimsey, R.G., 2013. Photogrammetric monitoring of lava dome growth during the 2009 eruption of Redoubt Volcano. J. Volcanol. Geotherm. Res. 259, 308–316. https://doi.org/10.1016/j.jvolgeores.2011.12.009.

Duffield, W.A., Dalrymple, G.B., 1990. The Taylor Creek Rhyolite of New Mexico: a rapidly emplaced field of lava domes and flows. Bull. Volcanol. 52, 475–487. https://doi.org/10.1007/BF00268927.

Dzurisin, D., Moran, S.C., Lisowski, M., Schilling, S.P., Anderson, K.R., Werner, C., 2015. The 2004–2008 dome-building eruption at Mount St. Helens, Washington: epilogue. Bull. Volcanol. 77. https://doi.org/10.1007/s00445-015-0973-4.

Eppler, D.B., Fink, J., Fletcher, R., 1987. Rheologic properties and kinematics of emplacement of the Chaos Jumbles rockfall avalanche, Lassen Volcanic National Park, California. J. Geophys. Res. 92, 3623–3633. https://doi.org/10.1029/JB092iB05p03623.

Farquharson, J.I., Wild, B., Kushnir, A.R.L., Heap, M.J., Baud, P., Kennedy, B., 2019. Acid-induced dissolution of andesite: evolution of permeability and strength. J. Geophys. Res. Solid Earth 124, 257–273. https://doi.org/10.1029/2018JB016130.

Fink, J.H., Bridges, N.T., 1995. Effects of eruption history and cooling rate on lava dome growth. Bull. Volcanol. 57, 229–239. https://doi.org/10.1007/BF00265423.

Fink, J.H., Griffiths, R.W., 1998. Morphology, eruption rates, and rheology of lava domes: Insights from laboratory models. J. Geophys. Res. 103, 527–545. https://doi.org/10.1029/97JB02838.

Fink, J.H., Kieffer, S.W., 1993. Estimate of pyroclastic flow velocities resulting from explosive decompression of lava domes. Nature 363, 612–615. https://doi.org/10.1038/363612a0.

Fink, J.H., Manley, C.R., 1987. Origin of pumiceous and glassy textures in rhyolite flows and domes. Spec. Pap. Geol. Soc. Am. 212, 77–88. https://doi.org/10.1130/SPE212-p77.

Fink, J.H., Malin, M.C., Anderson, S.W., 1990. Intrusive and extrusive growth of the Mount St Helens lava dome. Nature 348, 435–437. https://doi.org/10.1038/348435a0.

Ghorbani, A., Revil, A., Coperey, A., Soueid Ahmed, A., Roque, S., Heap, M.J., Grandis, H., Viveiros, F., 2018. Complex conductivity of volcanic rocks and the geophysical mapping of alteration in volcanoes. J. Volcanol. Geotherm. Res. 357, 106–127. https://doi.org/10.1016/j.jvolgeores.2018.04.014.

Griffiths, R.W., Fink, J.H., 1993. Effects of surface cooling on the spreading of lava flows and domes. J. Fluid Mech. 252, 667–702. https://doi.org/10.1017/S0022112093003933.

Hale, A.J., 2008. Lava dome growth and evolution with an independently deformable talus. Geophys. J. Int. 174, 391–417. https://doi.org/10.1111/j.1365-246X.2008.03806.x.

Hale, A.J., Wadge, G., 2008. The transition from endogenous to exogenous growth of lava domes with the development of shear bands. J. Volcanol. Geotherm. Res. 171, 237–257. https://doi.org/10.1016/j.jvolgeores.2007.12.016.

Hale, A.J., Bourgouin, L., Mühlhaus, H.B., 2007. Using the level set method to model endogenous lava dome growth. J. Geophys. Res. 112, B03213. https://doi.org/10.1029/2006JB004445.

Hale, A.J., Calder, E.S., Loughlin, S.C., Wadge, G., Ryan, G.A., 2009a. Modelling the lava dome extruded at Soufrière Hills Volcano, Montserrat, August 2005-May 2006. Part I: Dome shape and internal structure. J. Volcanol. Geotherm. Res. 187, 69–84. https://doi.org/10.1016/j.jvolgeores.2009.08.014.

Hale, A.J., Calder, E.S., Loughlin, S.C., Wadge, G., Ryan, G.A., 2009b. Modelling the lava dome extruded at Soufrière Hills Volcano, Montserrat, August 2005-May 2006. Part II: Rockfall activity and talus deformation. J. Volcanol. Geotherm. Res. 187, 69–84. https://doi.org/10.1016/j.jvolgeores.2009.08.014.

Harnett, C.E., Thomas, M.E., Purvance, M.D., Neuberg, J., 2018. Using a discrete element approach to model lava dome emplacement and collapse. J. Volcanol. Geotherm. Res. https://doi.org/10.1016/j.jvolgeores.2018.06.017.

Harnett, C.E., Kendrick, J.E., Lamur, A., Thomas, M.E., Stinton, A., Wallace, P.A., Utley, J.E.P., Murphy, W., Neuberg, J., Lavallée, Y., 2019a. Evolution of mechanical properties of lava dome rocks across the 1995–2010 eruption of soufrière hills volcano, Montserrat. Front. Earth Sci. 7. https://doi.org/10.3389/feart.2019.00007.

Harnett, C.E., Thomas, M.E., Calder, E.S., Ebmeier, S.K., Telford, A., Murphy, W., Neuberg, J., 2019b. Presentation and analysis of a worldwide database for lava dome collapse events: the Global Archive of Dome Instabilities (GLADIS). Bull. Volcanol. 81. https://doi.org/10.1007/s00445-019-1276-y.

Harnett, C.E., Heap, M.J., Thomas, M.E., 2020. A toolbox for identifying the expression of dome-forming volcanism on exoplanets. Planet. Space Sci. 180. https://doi.org/10.1016/j.pss.2019.104762.

Heap, M.J., Violay, M.E.S., 2021. The mechanical behaviour and failure modes of volcanic rocks: a review. Bull. Volcanol. 83. https://doi.org/10.1007/s00445-021-01447-2.

Heap, M.J., Lavallée, Y., Laumann, A., Hess, K.U., Meredith, P.G., Dingwell, D.B., 2012. How tough is tuff in the event of fire? Geology 40, 311–314. https://doi.org/10.1130/G32940.1.

Heap, M.J., Kennedy, B.M., Pernin, N., Jacquemard, L., Baud, P., Farquharson, J.I., Scheu, B., Lavallée, Y., Gilg, H.A., Letham-Brake, M., Mayer, K., Jolly, A.D., Reuschlé, T., Dingwell, D.B., 2015. Mechanical behaviour and failure modes in the Whakaari (White Island volcano) hydrothermal system, New Zealand. J. Volcanol. Geotherm. Res. 295, 26–42. https://doi.org/10.1016/j.jvolgeores.2015.02.012.

Heap, M.J., Coats, R., Chen, C. Feng, Varley, N., Lavallée, Y., Kendrick, J., Xu, T., Reuschlé, T., 2018. Thermal resilience of microcracked andesitic dome rocks. J. Volcanol. Geotherm. Res. 367, 20–30. https://doi.org/10.1016/j.jvolgeores.2018.10.021.

Heap, M.J., Troll, V.R., Kushnir, A.R.L., Gilg, H.A., Collinson, A.S.D., Deegan, F.M., Darmawan, H., Seraphine, N., Neuberg, J., Walter, T.R., 2019. Hydrothermal alteration of andesitic lava domes can lead to explosive volcanic behaviour. Nat. Commun. 10, 1–10. https://doi.org/10.1038/s41467-019-13102-8.

Heap, Michael J., Baumann, T., Gilg, H.A., Kolzenburg, S., Ryan, A.G., Villeneuve, M., Russell, J.K., Kennedy, L.A., Rosas-carbajal, M., Clynne, M.A., 2021a. Hydrothermal Alteration can Result in Pore Pressurization and Volcano Instability XX. pp. 1–5.

Heap, M.J., Baumann, T.S., Rosas-Carbajal, M., Komorowski, J., Gilg, H.A., Villeneuve, M., Moretti, R., Baud, P., Carbillet, L., Harnett, C., Reuschlé, T., 2021. Alteration-induced volcano instability at La Soufrière de Guadeloupe (Eastern Caribbean). J. Geophys. Res. Solid Earth 126, 1–23. https://doi.org/10.1029/2021jb022514.

Heap, Michael J., Wadsworth, F.B., Heng, Z., Xu, T., Grif, L., Aguilar, A., Vairé, E., Vistour, M., Reuschlé, T., Troll, V.R., Deegan, F.M., 2021b. The Tensile Strength of Volcanic Rocks : Experiments and Models. https://doi.org/10.1016/j.jvolgeores.2021.107348.

Herd, R.A., Edmonds, M., Bass, V., 2005. Catastrophic lava dome failure at Soufrière Hills Volcano, Montserrat, 12-13 July 2003. J. Volcanol. Geotherm. Res. 148, 234–252. https://doi.org/10.1016/j.jvolgeores.2005.05.003.

Holohan, E.P., Schöpfer, M.P.J., Walsh, J.J., 2011. Mechanical and geometric controls on the structural evolution of pit crater and caldera subsidence. J. Geophys. Res. Solid Earth 116, 1–23. https://doi.org/10.1029/2010JB008032.

Hungr, O., Leroueil, S., Picarelli, L., 2014. The Varnes classification of landslide types, an update. Landslides 11, 167–194. https://doi.org/10.1007/s10346-013-0436-y.

Huppert, H.E., Shepherd, J.B., Sigurdsson, H., Sparks, R.S.J., 1982. On lava dome growth, with application to the 1979 lava extrusion of the Soufrière of St. Vincent. J. Volcanol. Geotherm. Res. 14, 199–222. https://doi.org/10.1016/0377-0273(82)90062-2.

Husain, T., Elsworth, D., Voight, B., Mattioli, G.S., Jansma, P., 2014. Influence of extrusion rate and magma rheology on the growth of lava domes: Insights from particle-dynamics modeling. J. Volcanol. Geotherm. Res. 285, 110–117. https://doi.org/10.1016/j.jvolgeores.2014.08.013.

Hutchison, W., Varley, N., Pyle, D.M., Mather, T.A., Stevenson, J.A., 2013. Airborne thermal remote sensing of the Volcán de Colima (Mexico) lava dome from 2007 to 2010. Geol. Soc. London Spec. Publ. 380, 203–228. https://doi.org/10.1144/SP380.8.

Itasca Consulting Group, I, 2017. PFC2D (Particle Flow Code in Two Dimensions).

Kelfoun, K., Santoso, A.B., Latchimy, T., Bontemps, M., Nurdien, I., Beauducel, F., Fahmi, A., Putra, R., Dahamna, N., Laurin, A., Rizal, M.H., Sukmana, J.T., Gueugneau, V., 2021. Growth and collapse of the 2018–2019 lava dome of Merapi volcano. Bull. Volcanol. 83. https://doi.org/10.1007/s00445-020-01428-x.

Kereszturi, G., Schaefer, L.N., Miller, C., Mead, S., 2020. Hydrothermal alteration on composite volcanoes: mineralogy, hyperspectral imaging, and aeromagnetic study of Mt Ruapehu, New Zealand. Geochem. Geophys. Geosyst. 21, 0–3. https://doi.org/10.1029/2020GC009270.

Lamur, A., Lavallée, Y., Iddon, F.E., Hornby, A.J., Kendrick, J.E., Von Aulock, F.W., Wadsworth, F.B., 2018. Disclosing the temperature of columnar jointing in lavas. Nat. Commun. 9. https://doi.org/10.1038/s41467-018-03842-4.

Lavallée, Y., Varley, N.R., Alatorre-Ibargüengoitia, M.A., Hess, K.U., Kueppers, U., Mueller, S., Richard, D., Scheu, B., Spieler, O., Dingwell, D.B., 2012. Magmatic architecture of dome-building eruptions at Volcán de Colima, Mexico. Bull. Volcanol. 74, 249–260. https://doi.org/10.1007/s00445-011-0518-4.

Le Corvec, N., Muirhead, J.D., White, J.D.L., 2018. Shallow magma diversions during explosive diatreme-forming eruptions. Nat. Commun. 9, 1–8. https://doi.org/10.1038/s41467-018-03865-x.

Lesage, P., Carrara, A., Pinel, V., Arámbula-Mendoza, R., 2018. Absence of detectable precursory deformation and velocity variation before the large Dome Collapse of July 2015 at Volcán de Colima, Mexico. Front. Earth Sci. 6, 1–12. https://doi.org/10.3389/feart.2018.00093.

Maccaferri, F., Richter, N., Walter, T.R., 2017. The effect of giant lateral collapses on magma pathways and the location of volcanism. Nat. Commun. 8, 1–11. https://doi.org/10.1038/s41467-017-01256-2.

Macías, J.L., Siebe, C., 2005. Popocatépetl's crater filled to the brim: significance for hazard evaluation. J. Volcanol. Geotherm. Res. 141, 327–330. https://doi.org/10.1016/j.jvolgeores.2004.10.005.

Major, J.J., Dzurisin, D., Schilling, S.P., Poland, M.P., 2009. Monitoring lava-dome growth during the 2004-2008 Mount St. Helens, Washington, eruption using oblique terrestrial photography. Earth Planet. Sci. Lett. 286, 243–254. https://doi.org/10.1016/j.epsl.2009.06.034.

Manley, C.R., Fink, J.H., 1987. Internal textures of rhyolite flows as revealed by research drilling. Geology 15, 549–552. https://doi.org/10.1130/0091-7613(1987)15<549:ITORFA>2.0.CO;2.

Matthews, S.J., Gardeweg, M.C., Sparks, R.S.J., 1997. The 1984 to 1996 cyclic activity of Lascar Volcano, northern Chile: cycles of dome growth, dome subsidence, degassing and explosive eruptions. Bull. Volcanol. 59, 72–82. https://doi.org/10.1007/s004450050176.

Mendoza-Rosas, A.T., Gómez-Vázquez, Á., De la Cruz-Reyna, S., 2017. Statistical analysis of the sustained lava dome emplacement and destruction processes at Popocatépetl volcano, Central México. Bull. Volcanol. 79. https://doi.org/10.1007/s00445-017-1127-7.

Mordensky, S.P., Heap, M.J., Kennedy, B.M., Gilg, H.A., Villeneuve, M.C., Farquharson, J.I., Gravley, D.M., 2019. Influence of alteration on the mechanical behaviour and failure mode of andesite: implications for shallow seismicity and volcano monitoring. Bull. Volcanol. 81. https://doi.org/10.1007/s00445-019-1306-9.

Morgan, J.K., McGovern, P.J., 2005a. Discrete element simulations of gravitational volcanic deformation: 1. Deformation structures and geometries. J. Geophys. Res. B Solid Earth 110, 1–22. https://doi.org/10.1029/2004JB003252.

Morgan, J.K., McGovern, P.J., 2005b. Discrete element simulations of gravitational volcanic deformation: 2. Mechanical analysis. J. Geophys. Res. B Solid Earth 110, 1–13. https://doi.org/10.1029/2004JB003253.

Mueller, S.B., Varley, N.R., Kueppers, U., Lesage, P., Reyes Davila, Á.G., Dingwell, D.B., 2013. Quantification of magma ascent rate through rockfall monitoring at the growing/collapsing lava dome of Volcán de Colima, Mexico. Solid Earth 4, 201–213. https://doi.org/10.5194/se-4-201-2013.

Nagel, S.R., 1992. Instabilities in a sandpile. Rev. Mod. Phys. 64, 321–325. https://doi.org/10.1103/RevModPhys.64.321.

Ogburn, S.E., Loughlin, S.C., Calder, E.S., 2015. The association of lava dome growth with major explosive activity (VEI ≥ 4): DomeHaz, a global dataset. Bull. Volcanol. 77. https://doi.org/10.1007/s00445-015-0919-x.

Okubo, C.H., 2004. Rock mass strength and slope stability of the Hilina slump, Kilauea volcano, Hawai'i. J. Volcanol. Geotherm. Res. 138, 43–76. https://doi.org/10.1016/j.jvolgeores.2004.06.006.

Pérez, F.L., 1998. Talus fabric, clast morphology, and botanic indicators of slope processes on the Chaos Crags (California Cascades), U.S.A. Geogr. Phys. Quat. 52. https://doi.org/10.7202/004861ar.

Perras, M.A., Diederichs, M.S., 2014. A review of the tensile strength of rock: concepts and testing. Geotech. Geol. Eng. 32, 525–546. https://doi.org/10.1007/s10706-014-9732-0.

Potyondy, D.O., 2012. A flat-jointed bonded-particle material for hard rock. 46th US Rock Mech. Symp. 10.

Potyondy, D., 2016. Material-Modeling Support in PFC [Via fistPkg20].

Poulsen, B.A., Adhikary, D., Guo, H., 2018. Simulating mining-induced strata permeability changes. Eng. Geol. 237, 208–216. https://doi.org/10.1016/j.enggeo.2018.03.001.

Reid, M.E., Sisson, T.W., Brien, D.L., 2002. Volcano collapse promoted by hydrothermal alteration and edifice shape, Mount Rainier, Washington. Geology 29, 779–782. https://doi.org/10.1130/0091-7613(2001)029<0779:VCPBHA>2.0.CO;2.

Rhodes, E., Kennedy, B.M., Lavallée, Y., Hornby, A., Edwards, M., Chigna, G., 2018. Textural insights into the evolving Lava Dome Cycles at Santiaguito Lava Dome, Guatemala. Front. Earth Sci. 6, 1–18. https://doi.org/10.3389/feart.2018.00030.

Robertson, R., Cole, P.D., Sparks, R.S.J., Harford, C., Lejeune, A.M., Miller, A.D., Murphy, M.D., Norton, G., Stevens, N.F., 1998. The explosive eruption of Soufriere Hills Volcano, Montserrat, West Indies, 17 September, 1996. Geophys. Res. Lett. 25, 3429–3432. https://doi.org/10.1029/98GL01442.

Rosas-Carbajal, M., Komorowski, J.C., Nicollin, F., Gibert, D., 2016. Volcano electrical tomography unveils edifice collapse hazard linked to hydrothermal system structure and dynamics. Sci. Rep. 6, 1–11. https://doi.org/10.1038/srep29899.

Rosas-Carbajal, M., Jourde, K., Marteau, J., Deroussi, S., Komorowski, J.C., Gibert, D., 2017. Three-dimensional density structure of La Soufrière de Guadeloupe lava dome from simultaneous muon radiographies and gravity data. Geophys. Res. Lett. 44, 6743–6751. https://doi.org/10.1002/2017GL074285.

Ryan, A.G., Friedlander, E.A., Russell, J.K., Heap, M.J., Kennedy, L.A., 2018. Hot pressing in conduit faults during lava dome extrusion: Insights from Mount St. Helens 2004–2008. Earth Planet. Sci. Lett. 482, 171–180. https://doi.org/10.1016/j.epsl.2017.11.010.

Ryan, A.G., Heap, M.J., Russell, J.K., Kennedy, L.A., Clynne, M.A., 2020. Cyclic shear zone cataclasis and sintering during lava dome extrusion: Insights from Chaos Crags, Lassen Volcanic Center (USA). J. Volcanol. Geotherm. Res. 401, 106935. https://doi.org/10.1016/j.jvolgeores.2020.106935.

Schöpfer, M.P.J., Childs, C., Walsh, J.J., 2006. Localisation of normal faults in multilayer sequences. J. Struct. Geol. 28, 816–833. https://doi.org/10.1016/j.jsg.2006.02.003.

Schöpfer, M.P.J., Childs, C., Walsh, J.J., 2007. Two-dimensional distinct element modeling of the structure and growth of normal faults in multilayer sequences: 1. Model calibration, boundary conditions, and selected results. J. Geophys. Res. Solid Earth 112, 1–15. https://doi.org/10.1029/2006JB004902.

Sparks, R.S.J., Barclay, J., Calder, E.S., Herd, R.A., Komorowski, J.C., Luckett, R., Norton, G.E., Ritchie, L.J., Voight, B., Woods, A.W., 2002. Generation of a debris avalanche and violent pyroclastic density current on 26 December (Boxing Day) 1997 at Soufrière Hills Volcano, Montserrat. Geol. Soc. Lond. Mem. 21, 409–434. https://doi.org/10.1144/GSL.MEM.2002.021.01.18.

Stix, J., 1993. A model of degassing at Galeras Volcano, Colombia, 1988-1993. Geology 21, 963–967. https://doi.org/10.1130/0091-7613(1993)021<0963:AMODAG>2.3.CO;2.

Swanson, D.A., Dzurisin, D., Holcomb, R.T., Iwatsubo, E.Y., Chadwick, W.W., Casadevall, T.J., Ewert, J.W., Heliker, C.C., 1987. Growth of the lava dome at Mount St. Helens, Washington, (USA), 1981-1983. Geol. Soc. Am. Special Paper 1–16.

Szepesi, J., Lukács, R., Soós, I., Benkó, Z., Pécskay, Z., Ésik, Z., Kozák, M., Di Capua, A., Groppelli, G., Norini, G., Sulpizio, R., Harangi, S., 2019. Telkibánya lava domes: Lithofacies architecture of a Miocene rhyolite field (Tokaj Mountains, Carpathian-Pannonian region, Hungary). J. Volcanol. Geotherm. Res. 385, 179–197. https://doi.org/10.1016/j.jvolgeores.2019.07.002.

Taisne, B., Jaupart, C., 2008. Magma degassing and intermittent lava dome growth. Geophys. Res. Lett. 35, 1–5. https://doi.org/10.1029/2008GL035432.

Thomas, M.E., Petford, N., Bromhead, E.N., 2004. Volcanic rock-mass properties from Snowdonia and Tenerife: implications for volcano edifice strength. J. Geol. Soc. Lond. 161, 939–946. https://doi.org/10.1144/0016-764903-166.

Tuffen, H., James, M.R., Castro, J.M., Schipper, C.I., 2013. Exceptional mobility of an advancing rhyolitic obsidian flow at Cordón Caulle volcano in Chile. Nat. Commun. 4, 1–7. https://doi.org/10.1038/ncomms3709.

van Wyk de Vries, B., Francis, P.W., 1997. Catastrophic collapse at stratovolcanoes induced by gradual volcano spreading. Nature 387, 387–390. https://doi.org/10.1038/387387a0.

Van Wyk de Vries, B., Kerle, N., Petley, D., 2000. Sector collapse forming at Casita volcano, Nicaragua. Geology 28, 167–170. https://doi.org/10.1130/0091-7613(2000)28<167:SCFACV>2.0.CO;2.

Voight, B., Elsworth, D., 1997. Failure of volcano slopes. Géotechnique 47, 1–31. https://doi.org/10.1680/geot.1997.47.1.1.

Voight, B., Elsworth, D., 2000. Instability and collapse of hazardous gas-pressurized lava domes. Geophys. Res. Lett. 27, 1–4. https://doi.org/10.1029/1999GL008389.

Voight, B., Constantine, E.K., Siswowidjoyo, S., Torley, R., 2000. Historical eruptions of Merapi Volcano, Central Java, Indonesia, 1768-1998. J. Volcanol. Geotherm. Res. 100, 69–138. https://doi.org/10.1016/S0377-0273(00)00134-7.

Voight, B., Komorowski, J.-C., Norton, G.E., Belousov, A.B., Belousova, M., Boudon, G., Francis, P.W., Franz, W., Heinrich, P., Sparks, R.S.J., Young, S.R., 2002. The 26 December (Boxing Day) 1997 sector collapse and debris avalanche at Soufrière Hills Volcano, Montserrat. Geol. Soc. Lond. Mem. 21, 363–407. https://doi.org/10.1144/GSL.MEM.2002.021.01.17.

Voight, B., Linde, A.T., Sacks, I.S., Mattioli, G.S., Sparks, R.S.J., Elsworth, D., Hidayat, D., Malin, P.E., Shalev, E., Widiwijayanti, C., Young, S.R., Bass, V., Clarke, A., Dunkley, P., Johnston, W., McWhorter, N., Neuberg, J., Williams, P., 2006. Unprecedented pressure increase in deep magma reservoir triggered by lava-dome collapse. Geophys. Res. Lett. https://doi.org/10.1029/2005GL024870.

Wadge, G., Macfarlane, D.G., Odbert, H.M., James, M.R., Hole, J.K., Ryan, G., Bass, V., De Angelis, S., Pinkerton, H., Robertson, D.A., Loughlin, S.C., 2008. Lava dome growth and mass wasting measured by a time series of ground-based radar and seismicity observations. J. Geophys. Res. Solid Earth 113, 1–15. https://doi.org/10.1029/2007JB005466.

Wadge, G., Ryan, G., Calder, E.S., 2009. Clastic and core lava components of a silicic lava dome. Geology 37, 551–554. https://doi.org/10.1130/G25747A.1.

Walter, T.R., Ratdomopurbo, A., Subandriyo Aisyah, N., Brotopuspito, K.S., Salzer, J., Lühr, B., 2013. Dome growth and coulée spreading controlled by surface morphology, as determined by pixel offsets in photographs of the 2006 Merapi eruption. J. Volcanol. Geotherm. Res. 261, 121–129. https://doi.org/10.1016/j.jvolgeores.2013.02.004.

Walter, T.R., Harnett, C.E., Varley, N., Vargas, D., Salzer, J., Zorn, E.U., Bretón, M., Arámbula, R., Thomas, M.E., 2019. Imaging the 2013 explosive crater excavation and new dome formation at Volcán de Colima with TerraSAR-X, time-lapse cameras and modelling. J. Volcanol. Geotherm. Res. 369, 224–237. https://doi.org/10.1016/j.jvolgeores.2018.11.016.

Wang, T., Poland, M.P., Lu, Z., 2015. Dome growth at Mount Cleveland, Aleutian Arc, quantified by time series TerraSAR-X imagery. Geophys. Res. Lett. 1–8. https://doi.org/10.1002/2015GL066784.

Watters, R.J., Zimbelman, D.R., Bowman, S.D., Crowley, J.K., 2000. Rock mass strength assessment and significance to edifice stability, Mount Rainier and Mount Hood, Cascade Range volcanoes. Pure Appl. Geophys. 157, 957–976. https://doi.org/10.1007/s000240050012.

Watts, R.B., Herd, R.a., Sparks, R.S.J., Young, S.R., 2002. Growth patterns and emplacement of the andesitic lava dome at Soufrière Hills Volcano, Montserrat. Geol. Soc. Lond. Mem. 21, 115–152. https://doi.org/10.1144/GSL.MEM.2002.021.01.06.

Weaver, J., Eggertsson, G.H., Utley, J.E.P., Wallace, P.A., Lamur, A., Kendrick, J.E., Tuffen, H., Markússon, S.H., Lavallée, Y., 2020. Thermal liability of hyaloclastite in the Krafla geothermal reservoir, Iceland: the impact of phyllosilicates on permeability and rock strength. Geofluids 2020. https://doi.org/10.1155/2020/9057193.

Wensrich, C.M., Katterfeld, A., 2012. Rolling friction as a technique for modelling particle shape in DEM. Powder Technol. 217, 409–417. https://doi.org/10.1016/j.powtec.2011.10.057.

Williams, H., 1932. Geology of the Lassen Volcanic National Park. Univ. Calif. Publ. Geol. Sci. 21, 195–385.

Woods, A.W., Sparks, R.S.J., Ritchie, L.J., Batey, J., Gladstone, C., Bursik, M.I., 2002. The explosive decompression of a pressurized volcanic dome: the 26 December 1997 collapse and explosion of Soufrière Hills Volcano, Montserrat. Geol. Soc. Mem. 21, 457–465. https://doi.org/10.1144/GSL.MEM.2002.021.01.20.

Wu, S., Xu, X., 2016. A study of three intrinsic problems of the classic discrete element method using flat-joint model. Rock Mech. Rock. Eng. 49, 1813–1830. https://doi.org/10.1007/s00603-015-0890-z.

Wyering, L.D., Villeneuve, M.C., Wallis, I.C., Siratovich, P.A., Kennedy, B.M., Gravley, D.M., Cant, J.L., 2014. Mechanical and physical properties of hydrothermally altered rocks, Taupo Volcanic Zone, New Zealand. J. Volcanol. Geotherm. Res. 288, 76–93. https://doi.org/10.1016/j.jvolgeores.2014.10.008.

Young, S.R., Voight, B., Barclay, J., Herd, R.A., Komorowski, J.C., Miller, A.D., Sparks, R.S.J., Stewart, R.C., 2002. Hazard implications of small-scale edifice instability and sector collapse: a case history from Soufrière Hills Volcano, Montserrat. Geol. Soc. Mem. 21, 349–362. https://doi.org/10.1144/GSL.MEM.2002.021.01.16.

Závada, P., Kratinová, Z., Kusbach, V., Schulmann, K., 2009. Internal fabric development in complex lava domes. Tectonophysics 466, 101–113. https://doi.org/10.1016/j.tecto.2008.07.005.

Zorn, E.U., Rowe, M.C., Cronin, S.J., Ryan, A.G., Kennedy, L.A., Russell, J.K., 2018. Influence of porosity and groundmass crystallinity on dome rock strength: a case study from Mt. Taranaki, New Zealand. Bull. Volcanol. 80. https://doi.org/10.1007/s00445-018-1210-8.

Zorn, E.U., Le Corvec, N., Varley, N.R., Salzer, J.T., Walter, T.R., Navarro-Ochoa, C., Vargas-Bracamontes, D.M., Thiele, S.T., Arámbula Mendoza, R., 2019. Load stress controls on directional lava dome growth at volcán de Colima, Mexico. Front. Earth Sci. 7, 1–18. https://doi.org/10.3389/feart.2019.00084.

Zorn, E.U., Walter, T.R., Heap, M.J., Kueppers, U., 2020a. Insights into lava dome and spine extrusion using analogue sandbox experiments. Earth Planet. Sci. Lett. 551, 116571. https://doi.org/10.1016/j.epsl.2020.116571.

Zorn, E.U., Walter, T.R., Johnson, J.B., Mania, R., 2020b. UAS-based tracking of the Santiaguito Lava Dome, Guatemala. Sci. Rep. 10, 1–13. https://doi.org/10.1038/s41598-020-65386-2.